



Technical note

Feasibility of the J-PET to monitor the range of therapeutic proton beams

Jakub Baran^{a,b,c,*}, Damian Borys^{d,e,f}, Karol Brzeziński^{f,g}, Jan Gajewski^f, Michał Silarski^{a,b,c}, Neha Chug^{a,b,c}, Aurélien Coussat^{a,b,c}, Eryk Czerwiński^{a,b,c}, Meysam Dadgar^{a,b,c}, Kamil Dulski^{a,b,c}, Kavya V. Eliyan^{a,b,c}, Aleksander Gajos^{a,b,c}, Krzysztof Kacprzak^{a,b,c}, Łukasz Kapłon^{a,b,c}, Konrad Klimaszewski^h, Paweł Konieczka^h, Renata Kopeć^f, Grzegorz Korcyl^{a,b,c}, Tomasz Kozik^{a,b,c}, Wojciech Krzemieńⁱ, Deepak Kumar^{a,b,c}, Antony J. Lomax^{l,m}, Keegan McNamara^{l,m}, Szymon Niedźwiecki^{a,b,c}, Paweł Olko^f, Dominik Panek^{a,b,c}, Szymon Parzych^{a,b,c}, Elena Perez del Rio^{a,b,c}, Lech Raczyński^h, Moyo Simbarashe^{a,b,c}, Sushil Sharma^{a,b,c}, Shivani^{a,b,c}, Roman Y. Shopa^h, Tomasz Skóraⁿ, Magdalena Skurzok^{a,b,c}, Paulina Stasica^f, Ewa Ł. Stępień^{a,b,c}, Keyvan Tayefi^{a,b,c}, Faranak Tayefi^{a,b,c}, Damien C. Weber^{j,k,l}, Carla Winterhalter^{l,m}, Wojciech Wiślicki^h, Paweł Moskal^{a,b,c}, Antoni Ruciński^f

^a Faculty of Physics, Astronomy and Applied Computer Science, Jagiellonian University, 11 Łojasiewicza St 30-348 Kraków, Poland

^b Total-Body Jagiellonian-PET Laboratory, Jagiellonian University, 30-348 Kraków, Poland

^c Center for Theranostics, Jagiellonian University, Kraków, Poland

^d Silesian University of Technology, Department of Systems Biology and Engineering, Gliwice, Poland

^e Biotechnology Centre, Silesian University of Technology, Gliwice, Poland

^f Institute of Nuclear Physics Polish Academy of Sciences, 31-342, Kraków, Poland

^g Instituto de Física Corpuscular (IFIC), CSIC-UV, Valencia, Spain

^h Department of Complex Systems, National Centre for Nuclear Research, Otwock-Świerk, Poland

ⁱ High Energy Physics Division, National Centre for Nuclear Research, Otwock-Świerk, Poland

^j Department of Radiation Oncology, Inselspital, Bern University Hospital, University of Bern, Bern, Switzerland

^k Department of Radiation Oncology, University Hospital of Zürich, Zürich Switzerland

^l Centre for Proton Therapy, Paul Scherrer Institute, Villigen, Switzerland

^m Physics Department, ETH Zürich, Zürich, Switzerland

ⁿ National Oncology Institute, National Research Institute, Krakow Branch, Krakow, Poland

ARTICLE INFO

Keywords:

PET
Range monitoring
J-PET
Monte Carlo simulations
Proton radiotherapy

ABSTRACT

Purpose: The aim of this work is to investigate the feasibility of the Jagiellonian Positron Emission Tomography (J-PET) scanner for intra-treatment proton beam range monitoring.

Methods: The Monte Carlo simulation studies with GATE and PET image reconstruction with CASToR were performed in order to compare six J-PET scanner geometries. We simulated proton irradiation of a PMMA phantom with a Single Pencil Beam (SPB) and Spread-Out Bragg Peak (SOBP) of various ranges. The sensitivity and precision of each scanner were calculated, and considering the setup's cost-effectiveness, we indicated potentially optimal geometries for the J-PET scanner prototype dedicated to the proton beam range assessment.

Results: The investigations indicate that the double-layer cylindrical and triple-layer double-head configurations are the most promising for clinical application. We found that the scanner sensitivity is of the order of 10^{-5} coincidences per primary proton, while the precision of the range assessment for both SPB and SOBP irradiation plans was found below 1 mm. Among the scanners with the same number of detector modules, the best results are found for the triple-layer dual-head geometry. The results indicate that the double-layer cylindrical and triple-layer double-head configurations are the most promising for the clinical application.

Conclusions: We performed simulation studies demonstrating that the feasibility of the J-PET detector for PET-based proton beam therapy range monitoring is possible with reasonable sensitivity and precision enabling its pre-clinical tests in the clinical proton therapy environment. Considering the sensitivity, precision and

* Corresponding author at: Faculty of Physics, Astronomy and Applied Computer Science, Jagiellonian University, 11 Łojasiewicza St 30-348 Kraków, Poland.
E-mail address: jakubbaran92@gmail.com (J. Baran).

cost-effectiveness, the double-layer cylindrical and triple-layer dual-head J-PET geometry configurations seem promising for future clinical application.

1. Introduction

Radiation therapy is frequently applied for cancer treatment. Proton therapy offers an advantageous depth dose characteristic making protons a popular treatment choice for selected, often deeply seated tumors located in proximity of critical organs at risk (OAR) [1–3]. However, a significant limitation is the uncertainty in precise determining the range of the proton beam that can result in underdosage of treatment volume or overdosage of critical structure. One approach to overcome this problem is the in vivo verification of the radiation delivery by monitoring beam range. As the primary protons stop in the patient's body, monitoring techniques based on measurement of the secondary particles, i.e., prompt gamma imaging [4–7], secondary charged particles tracking [8–11], and positron emission tomography (PET) [12–15] have been proposed and tested pre-clinically and clinically. Range monitoring may motivate the interruption of the beam delivery once the proton range differs from the one prescribed in the treatment plan, and be followed by online treatment adaptation, particularly when hypofractionation or FLASH modality are applied.

The application of PET for proton range monitoring consists of imaging β^+ -emitting isotopes, such as ^{11}C ($T_{1/2}=20.4$ min), ^{10}C ($T_{1/2}=19$ s) or ^{15}O ($T_{1/2}=2$ min), produced during the nuclear interactions of protons with the tissues in the patient. Due to patient positioning uncertainties and washout effects, favourably, PET imaging should be performed in the treatment room, during or just after the irradiation.

Different PET scanner geometries have been introduced and tested, both experimentally and using Monte Carlo simulations, starting from commercially available PET scanners mounted out of the treatment room [16], towards more compact prototype solutions equipped with fast and sophisticated data acquisition systems, and installed in the treatment room, sharing space with gantry nozzle and treatment couch.

These included dual-head scanners [14,17–19] or more sophisticated configurations such as the axially shifted, single-ring OpenPET [20,21] or the axially slanted full-ring and dual-ring [22,23] configurations.

To meet the requirements placed on PET-based range monitoring systems in proton radiation therapy, the Jagiellonian Positron Emission Tomography (J-PET) scanner [24,25], a novel, cost-effective, portable, modular PET scanner, based on plastic scintillator technology, is being considered for this application. Here, we present for the first time a feasibility study of the different J-PET geometries for the application of proton beam range verification. We performed Monte Carlo simulations in homogeneous media to compare six geometries (three dual-heads and three cylindrical), which could be potentially considered for beam range monitoring in the treatment room. We report the relative efficiency of the scanners for Single Pencil Beam (SPB) and Spread-Out Bragg Peak (SOBP) irradiation plans. Quantitative analysis is conducted to assess the precision of range detection in two acquisition protocols with uniform phantoms and different scanner geometries, and to eventually indicate the optimal J-PET configuration for proton beam range monitoring.

2. Materials and methods

2.1. J-PET scanner and geometries for proton therapy range monitoring

The existing prototype of the J-PET scanner and the schematic illustration of its operation principle is presented in Fig. 1. The disadvantage of the plastic scintillators with respect to the conventionally used crystal scintillations, is their efficiency [26] which in the case of the proton range monitoring is enhanced as the expected statistics is

far beyond the level of clinical activities. Considering that the plastics scintillators are relatively cheap and have photomultipliers at their ends, the improvement in PET signal quality could be achieved by an increase of the thickness of the plastic scintillator, adding subsequent layers of plastic modules or increasing the length of the scintillators to enlarge the Field-Of-View (FOV) [27]. Applying any of these approaches will increase the price of the system. However, the increase is not as substantial as for the organic scintillators [26,28]. The J-PET technology cost-effectiveness, portability, and the possibility to build various geometries with the same amount of modules make the J-PET scanner promising for proton range monitoring. Additionally, the J-PET could also be applied with success in Total-Body PET imaging [25,28,29], multi-gamma tomography using, e.g., positronium imaging [30,31], fundamental physics studies on quantum entanglement [32,33], studies of discrete symmetries in nature [24] or PET data reconstruction methods development [34,35]. Moreover, plastic scintillators in J-PET are characterized by short light signals with a decay constant of about 2 ns (factor of 20 to 150 less than these of crystal detectors) [25]. Therefore J-PET has two orders of magnitudes reduced probability for signal pile-ups with respect to crystal PET systems, making it especially promising for monitoring of high dose rate flash radiotherapy [36].

The modular J-PET technology (as presented in Fig. 1) was developed to allow its reconfiguration for different applications. The J-PET module is built out of 13 separate 50 cm long scintillator strips, each having a cross-section of 6×24 mm². Individual scintillators are covered with kapton and reflective foils [37,38]. Each of the 13 scintillation strips is connected to 8 SiPMs, 4 at each side of the strip, which convert the light into an electronic signal, further processed with the FPGA electronics [39].

For the purpose of proton therapy range monitoring, we propose and investigate six PET scanner configurations, built from the J-PET modules (Fig. 2). The PET geometries can be classified as two general types: the cylindrical (Fig. 2A–C) and the dual-head (Fig. 2D–F) configurations, each of them in a single-, dual-, and triple-layer geometry. The cylindrical setup could be used in the therapy room, whereas dual-head setups could be potentially also considered for the in-beam or inter-spill scenarios [40–42]. Each layer of the multi-layer cylindrical system consisted of 24 modules. The dual-head configurations consisted of 12, 24 and 24 modules for single, double and triple layer setups, respectively. The radius of the system, defined as the distance between the isocenter and the surface of the innermost strip in the module, was equal to 369.9 mm and 300.0 mm for cylindrical and dual-head configurations, respectively. The gap between adjacent layers was fixed to 44 mm for all setups.

The modules in the cylindrical configurations were positioned parallel to the beam direction. In contrast, the modules in dual-head configurations were positioned perpendicular to the beam, motivated by the potential improvement of the J-PET detector resolution in the direction perpendicular to the strips. When the modules are positioned parallel to the beam direction (cylindrical setups), the precision of the range measurement depends on the resolution of the interaction position along the strip, which is determined by the detector's timing properties [27]. On the other hand, for the dual-head configurations, the range measurement depends on the resolution determined by the width of the plastic strips (6 mm), which is superior to that along the strip length.

2.2. Monte Carlo simulations

In this work, we exploited Monte Carlo methods for simulation and evaluation of the feasibility of various J-PET geometries for proton therapy range monitoring. We used the ProTheRaMon software

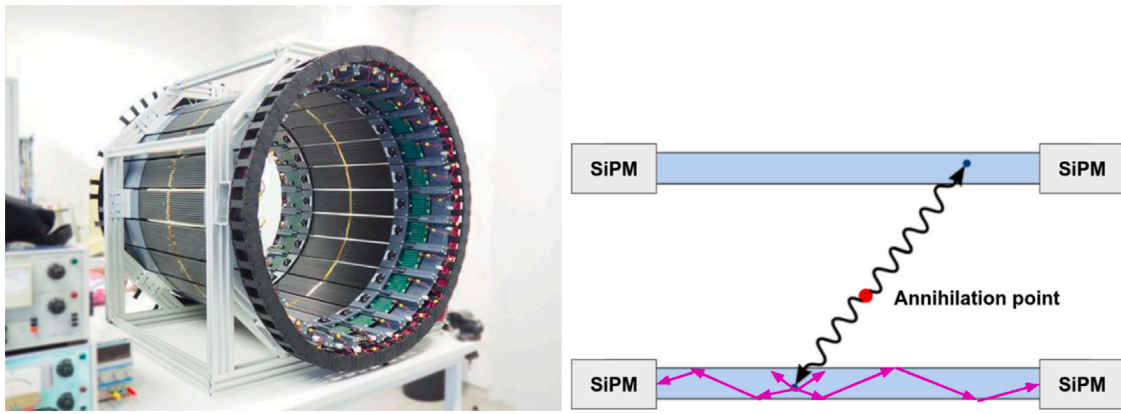


Fig. 1. The modular J-PET scanner (left panel) developed as a cost-effective, diagnostic total-body PET prototype that was investigated in this study for intra-treatment proton therapy range monitoring. The presented geometry corresponds to the single layer cylindrical configuration (see Fig. 2 A). The principle of annihilation gamma-rays detection with the J-PET module is illustrated in the right panel. Annihilation gamma-rays (black arrows) create in the plastic scintillator photons (magenta arrows) which propagate to the ends of the strip and are converted to the electronics signals by the silicon photomultipliers (SiPM).

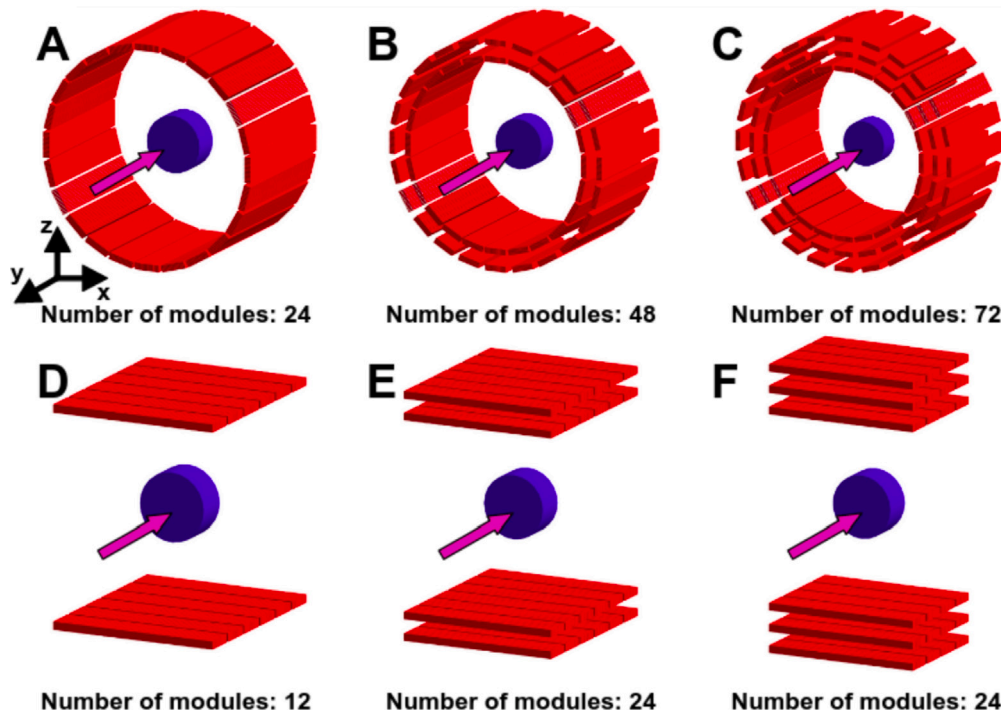


Fig. 2. The J-PET based geometrical configurations proposed for application in proton therapy range monitoring. In the Monte Carlo simulation study presented here we investigated: single layer cylinder (A), double layer cylinder (B), triple layer cylinder (C), single layer dual-head (D), double layer dual-head (E), and triple layer dual-head (F) configurations. A cylindrical water (blue) phantom was isocentrally positioned inside each of the configurations. The number of modules per layer in each head for single, double and triple layer dual-head setups is 6, 6 and 4, respectively. Purple arrows show the direction of the proton beam.

framework, in which the delivery of proton therapy treatment plans, scoring the β^+ activity produced by protons during the treatment, as well as the J-PET scanner response to the annihilation gammas [43] were simulated.

For simulations of the treatment plan irradiation, we used the Geant4 QGSP_BIC_HP_EMY physics list with the RadioactiveDecay model. The beam model of the Cyclotron Centre Bronowice (CCB) Krakow proton therapy centre, along with the CT calibration, were implemented as described in [44]. For the simulation of the two 511 keV photon propagation from the positron–electron annihilation position to the PET scanner and their interaction with the plastic scintillator, the emlvmore_polar physics list was used. We did not simulate scintillation processes, but we considered the energetic resolution of the scintillators [25] calculated based on experimental measurements, performed for the plastic scintillator strips [45]. The fractional energy

resolution for the energy deposited by the annihilation quanta is equal to 7.5% at the Compton edge. A 200–380 keV energy window was set to extract a list of the coincidences, along with a 3 ns time window [25].

In this study, we simulated the irradiation of a PMMA phantom with proton SPB and SOBPs of various ranges, and data acquisition protocols to investigate the feasibility of different J-PET geometries for proton range monitoring. All treatment plans were optimized in the Varian Eclipse 16.1 treatment planning system, used routinely in CCB for patient treatment planning.

The SPB plans were prepared with nominal proton energies of 125.68 MeV, 127.15 MeV, 129.34 MeV, and 132.25 MeV, irradiating a $5 \times 20 \times 5 \text{ cm}^3$ PMMA phantom, achieving the corresponding Bragg peak range of 100 mm, 102 mm, 105 mm, and 109 mm, respectively. The plans were normalized to 8 Gy in the Bragg peak maximum, which corresponds to about $3.3 \cdot 10^9$ primary protons.

Three sets of SOBP plans were prepared to obtain homogeneous dose distributions in $3 \times 3 \times 3 \text{ cm}^3$, $5 \times 5 \times 5 \text{ cm}^3$, and $7 \times 7 \times 7 \text{ cm}^3$ cubes, inside a $20 \times 15 \times 20 \text{ cm}^3$ PMMA phantom. Each of these sets was optimized to obtain the SOBP range the same as for the SPB plans, i.e. 100 mm, 102 mm, 105 mm, and 109 mm, leading to 12 SOBP plans of varying volume and range. The plans were normalized to 4 Gy(RBE) in the SOBP cube, leading the total number of primaries of about $4.0 \cdot 10^{10}$, $9.6 \cdot 10^{10}$, and $2.1 \cdot 10^{11}$, for the small, medium, and large cubes, respectively. Both, the SPB and SOBP plans were irradiated along the y direction of the corresponding phantom (see Fig. 2).

For the simulation of 511 keV annihilation photons propagation, the phantoms were positioned isocentrically inside the PET scanners. We assumed the in-room PET acquisition to start 90 s after the end of the irradiation and last for 120 s.

2.3. PET image reconstruction

The CASToR software [46] v. 3.1 was used for the PET data reconstruction. Since CASToR does not allow TOF modelling of the scintillation quanta propagation along the plastic scintillator strips, these were discretized to 100 artificial scintillators ($6 \times 24 \times 5 \text{ mm}^3$) along the longest dimension of the plastic strip. This discretization corresponds to the TOF resolution ($FWHM = 5 \text{ mm}$) along the J-PET strips [25,47]. The list-mode TOF MLEM reconstruction algorithm was used with TOF resolution equal to 500 ps (FWHM) and with Siddon projector. Reconstructed images were corrected for sensitivity and attenuation. The PMMA linear attenuation coefficient was set to 0.104 cm^{-1} . Reconstruction voxel was 2.5 mm^3 , isotropic. The reconstructed FOV was restricted to the phantom size ($5 \times 20 \times 5 \text{ cm}^3$ for SPB and $20 \times 15 \times 20 \text{ cm}^3$ for SOBP) to speed up the reconstruction. The reconstructed images were smoothed with the 3D Gaussian filter with $\sigma=1$ voxel [18]. The images were reconstructed with 3 iterations.

2.4. Analysis

The comparison of J-PET setup configurations was conducted for both, SPB and SOBP simulations, considering (i) the sensitivity, and (ii) the precision of range shift detection.

We defined the sensitivity, denoted η , as the ratio of the number of detected coincidence events per primary proton. It was calculated for each geometry and SPB/SOBP of different range. The η factor is given as:

$$\eta = \frac{c}{p}, \quad (1)$$

where c is the number of registered coincidences and p is the number of simulated primary protons. In order to compare the six J-PET configurations, we defined and calculated the geometry-dependent normalized sensitivity factor H given as:

$$H = \frac{\eta_{geom}}{\eta_{ref}}, \quad (2)$$

where the η_{geom} is calculated for the investigated simulation setup (considering both SPB and SOBP simulations) and η_{ref} is calculated for the single layer cylindrical geometry.

The mean value \bar{H} was calculated separately for the SPB and SOBP studies for each geometry. For the SPB \bar{H} was averaged over 4 beam ranges and for the SOBP over 4 beam ranges and 3 different dose cube sizes. The \bar{H} values were compared between the scanners for each simulation scenario separately.

We also performed a quantitative analysis of the precision which can be expected for detecting proton beam range with different J-PET geometry configurations. The dose range, R_D , was calculated as the depth of 80% of the distal fall-off of the integral depth dose (IDD) profile of SPB or central axis profile of SOBP, as we found that analysis method does not influence the estimation of the distal fall-off position. Combinations of four dose ranges of SPB or SOBP, i.e. R_D were equal to

Table 1

The sensitivity η and normalized sensitivity factor \bar{H} for SPB and SOBP irradiations computed for the investigated J-PET geometries. The reference geometry is the single layer cylindrical setup.

Setup	SPB			SOBP		
	$\eta[10^{-6}]$	$\sigma(\eta)[10^{-6}]$	\bar{H}	$\eta[10^{-6}]$	$\sigma(\eta)[10^{-6}]$	\bar{H}
Single layer cylindrical	9.45	0.29	1.0	3.64	0.22	1.0
Double layer cylindrical	27.41	0.80	2.9	10.76	0.65	2.9
Triple layer cylindrical	45.72	1.26	4.8	18.00	1.11	5.0
Single layer dual-head	3.79	0.13	0.4	2.45	0.19	0.7
Double layer dual-head	10.55	0.35	1.1	7.21	0.56	2.0
Triple layer dual-head	10.22	0.26	1.1	8.92	0.78	2.4

100 mm, 102 mm, 104 mm, and 109 mm, allowed to analyse six dose range differences, δR_D , i.e. 2 mm, 3 mm, 4 mm, 5 mm, 7 mm, and 9 mm. The differences in dose range, δR_D , of SPB or SOBP irradiations were assumed to be the reference for the activity range analysis.

The activity range, R_A [48], was calculated by fitting a sigmoid function to the distal fall-off of the 3D activity distribution reconstructed with a given J-PET geometry. Based on the fit, the R_A was determined at 50% of the distal fall-off maximum [49–51]. The difference of six activity ranges, δR_A , associated with the six reference differences in dose range, δR_D , was calculated by subtracting the range of fitted activity profiles. The deviation between activity and dose range difference, ΔR , was individually calculated for each geometry setup and for SPB and SOBP, as:

$$\Delta R = \delta R_D - \delta R_A. \quad (3)$$

Note that for a PET scanner that flawlessly reconstructs the emission activity distribution, the ΔR is expected to be equal to zero.

We calculated the uncertainty of the deviation between activity and dose range difference (ΔR) for each investigated scanner geometry and for SPBs and SOBPs of different field size. For this purpose, the mean $\bar{\Delta R}$ and standard deviation $\sigma \Delta R$ of ΔR was calculated, $\sigma \Delta R$ being proposed as a metric of the precision of the activity range detection.

3. Results

3.1. Sensitivity

The ratio of detected coincidence events per primary proton (η), and the normalized sensitivity factor (\bar{H}), all computed for SPB and SOBP irradiations in six J-PET geometries are given in Table 1. The η factor for the SPB ranges from $0.4 \cdot 10^{-5}$ to $4.8 \cdot 10^{-5}$ for single layer dual-head and triple layer cylindrical setups, respectively. For the SOBP the numbers are smaller due to the bigger phantom (greater attenuation) and range from $0.25 \cdot 10^{-5}$ to $2.0 \cdot 10^{-5}$ for single layer dual-head and triple layer cylindrical setups, respectively. The greatest value of \bar{H} is observed for the triple and double layer cylindrical setups and the lowest for the single layer dual-head. For the SBP irradiation, the sensitivity of the J-PET geometries consisting of the same number of modules, i.e., single layer cylindrical, double layer dual-head and triple layer dual-head is comparable within about 10%. However, for the SOBP scenario, the geometry-specific sensitivity factor \bar{H} varies significantly (about 2–2.4 times) for double and triple layer dual-head setups with respect to the single layer cylindrical geometry. It shows the advantage of adding the subsequent detector layers over the greater coverage of the FOV when the same number of modules is available. For the cylindrical setups, the addition of the new layer of modules increases the sensitivity of the system.

3.2. Examples of reconstructed activity distributions and profiles

We selected exemplary images for cylindrical and dual-head configurations considering the sensitivity (\bar{H} factor) and cost-effectiveness of

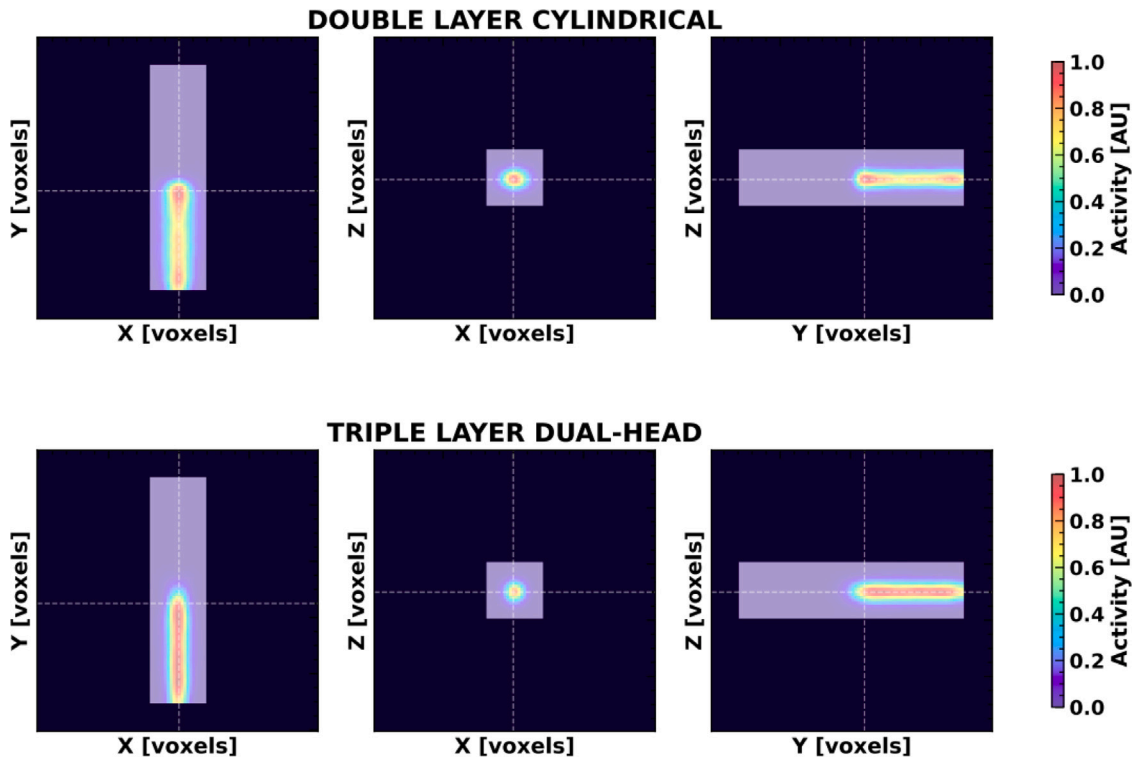


Fig. 3. Example of the reconstructed PET images resulting from the SPB irradiation at 125.68 MeV and range of 100 mm. The activity distributions reconstructed with 3 iterations are shown for the double layer cylindrical (top row) and triple layer dual-head (bottom row) geometries. Post-reconstruction 3D Gaussian smoothing of the activity distribution with σ equal to 1 voxel was applied. The PMMA phantom size is $5 \times 20 \times 5 \text{ mm}^3$. The voxel size is $2.5 \times 2.5 \times 2.5 \text{ mm}^3$.

the setup. For the cylindrical setup, the \bar{H} factor increases by about 300% between single (24 modules) and double layer (48 modules) configuration, while increasing only by about 70% from the double (48 modules) and triple layer (72 modules) configuration. We, therefore, consider the double layer geometry as the more cost-effective solution for the cylindrical configuration [25,43]. The triple layer dual-head is characterized by the highest \bar{H} factor and is constructed of only 24 modules.

Reconstructed PET images from the double layer cylindrical and triple layer dual-head geometry, for SBP and SOBP irradiations, are shown in Fig. 3 and Fig. 4, respectively. For both geometries, the relation between reconstructed images and the corresponding dose, production, and emission distributions, was previously shown in Borys et al. 2022 [43]. It could be found that the triple layer dual-head geometry setups do not suffer from missing projection artefacts. The reason is limited reconstruction FOV to the phantom region only, using the TOF information and the smoothing procedure applied to the reconstructed image. Furthermore, in Fig. 5 we show an example of profiles taken through images reconstructed following the SPB and SOBP irradiations, together with the fitted sigmoid functions, as well as the corresponding emission profiles for comparison. As in Figs. 3 and 4, only the double layer cylindrical and triple layer dual-head configurations are shown.

Note that the fall-off reconstructed image profiles for the SBP irradiations are qualitatively more similar to the emission fall-offs than the fall-offs obtained from the SOBP irradiations.

3.3. Precision of range shift detection with various J-PET geometries

Figs. 6 and 7 show ΔR , the difference between the range shift in the dose and the range shift as measured from the reconstructed activity distributions after fitting the sigmoid function, for simulations of SPB and SOBP field irradiations, respectively. The figures have six panels, each of them showing the results for one of the investigated geometrical

Table 2

Calculated distances between measured and reference difference for the SPB and SOBP study.

Setup	SPB study		SOBP study	
	$\overline{\Delta R}$ [mm]	$\sigma_{\Delta R}$ [mm]	$\overline{\Delta R}$ [mm]	$\sigma_{\Delta R}$ [mm]
Single layer cylindrical	0.22	0.26	0.10	0.50
Double layer cylindrical	0.45	0.27	0.17	0.36
Triple layer cylindrical	0.40	0.27	0.31	0.64
Single layer dual-head	0.79	0.58	0.07	0.83
Double layer dual-head	0.33	0.42	-0.37	0.43
Triple layer dual-head	-0.06	0.04	-0.05	0.56

configurations of the J-PET scanner. For the SOBP irradiations, the results for three irradiation fields of different sizes are given. Additionally, in Table 2 calculated mean and standard deviation values are given separately for the SPB and SOBP irradiation.

The mean of the differences in range shift, between the reference and the measurements made on reconstructed images, ranges from -0.37mm to 0.85 mm. These values are smaller than the voxel size of the reconstructed PET image (isotropic 2.5 mm). The standard deviation of ΔR , which we associate with the precision of the range detection, is below 1 mm for both, SPB and SOBP irradiations. For all the investigated geometries, higher precision is observed for the SPB than SOBP. The best precision for the SPB is found for the triple layer dual-head and the worst for the single layer dual-head. All cylindrical configurations show similar precision for the SPB investigation. Among the dual-head setups, the single layer geometry has the worst results for both SOBP and SPB studies.

Comparing the geometries with the same number of modules, for the SPB the best range detection precision was found for the triple layer dual-head, whereas for the SOBP the double layer dual-head configurations was found to be superior.

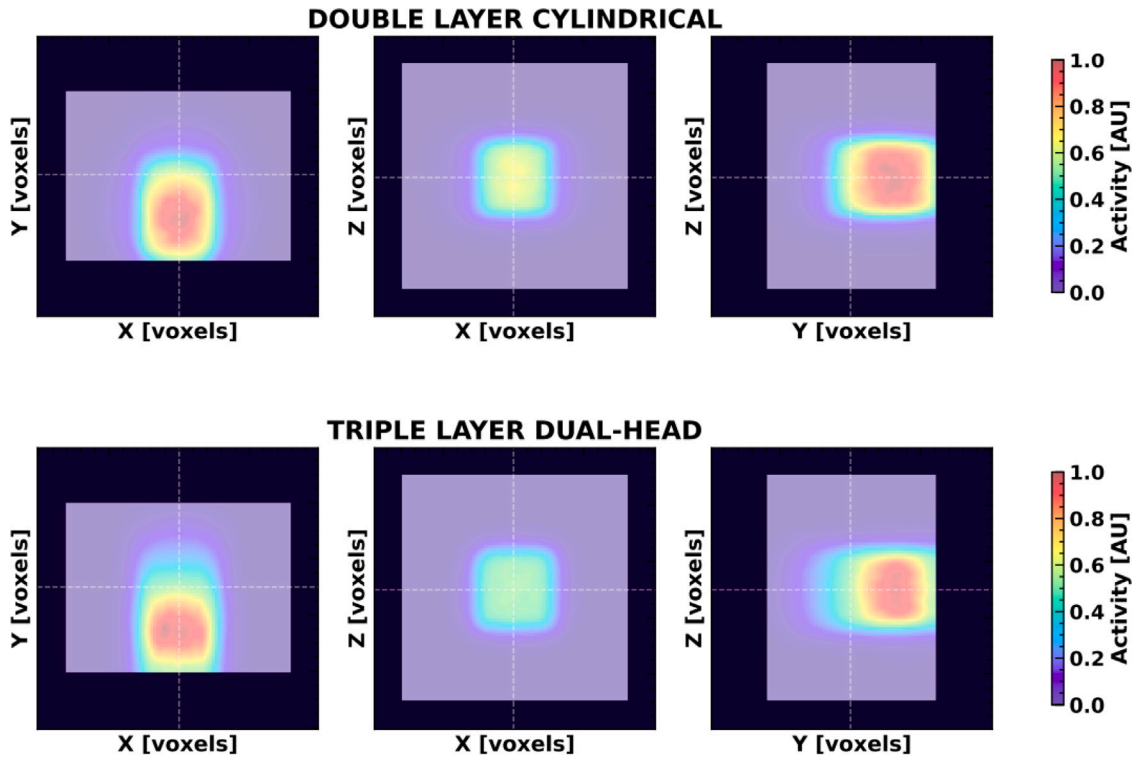


Fig. 4. Example of the reconstructed PET images resulting from irradiation of the SOBp of $5 \times 5 \times 5 \text{ cm}^3$ and 100 mm range. The activity distributions reconstructed with 3 iterations are shown for the double layer cylindrical (top row) and triple layer dual-head (bottom row) geometries. Post-reconstruction 3D Gaussian smoothing of the activity distribution with σ equal to 1 voxel was applied. The PMMA phantom size is $20 \times 15 \times 20 \text{ mm}^3$. The voxel size is $2.5 \times 2.5 \times 2.5 \text{ mm}^3$.

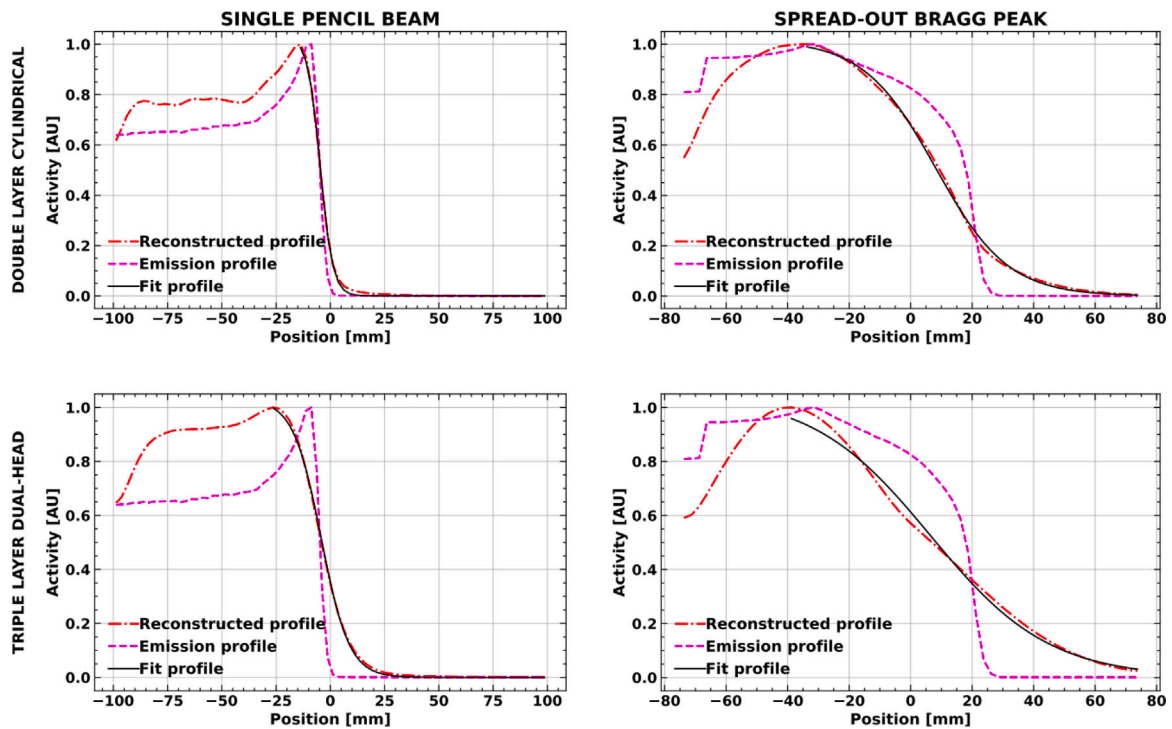


Fig. 5. Examples of emission profiles, reconstructed activity profiles and sigmoid function fitted to the reconstructed profiles for SPB (left column) and SOBp irradiations (right column) for double layer cylindrical (top row) and triple layer dual-head (bottom row) geometry configurations.

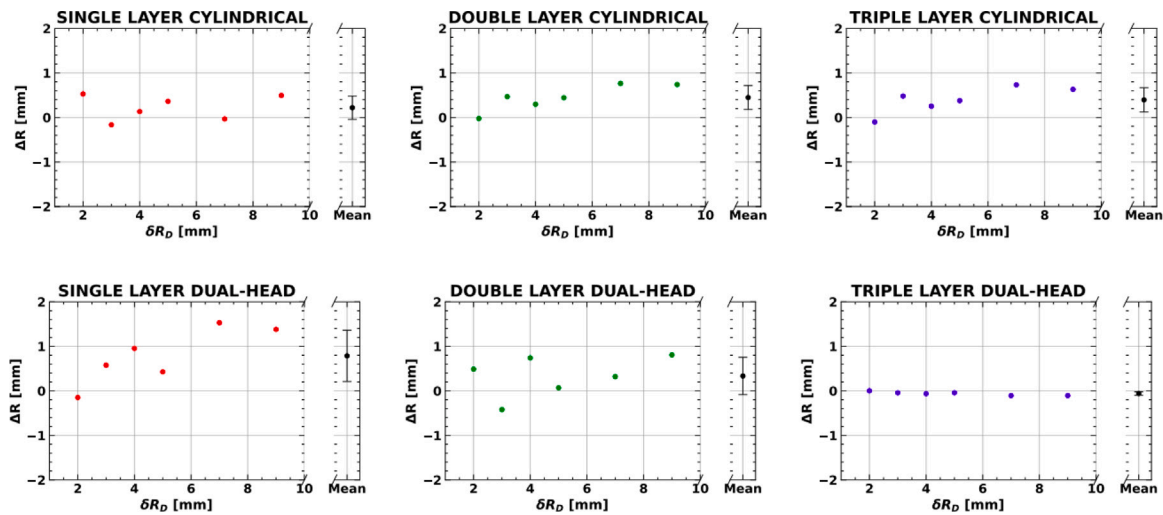


Fig. 6. ΔR for all six geometries of the J-PET scanner investigated for SPB irradiations. Top row shows the results for cylindrical geometries and the bottom for the dual-head setups. The columns from left to right present the results for the single, double and triple layer scanner geometries.

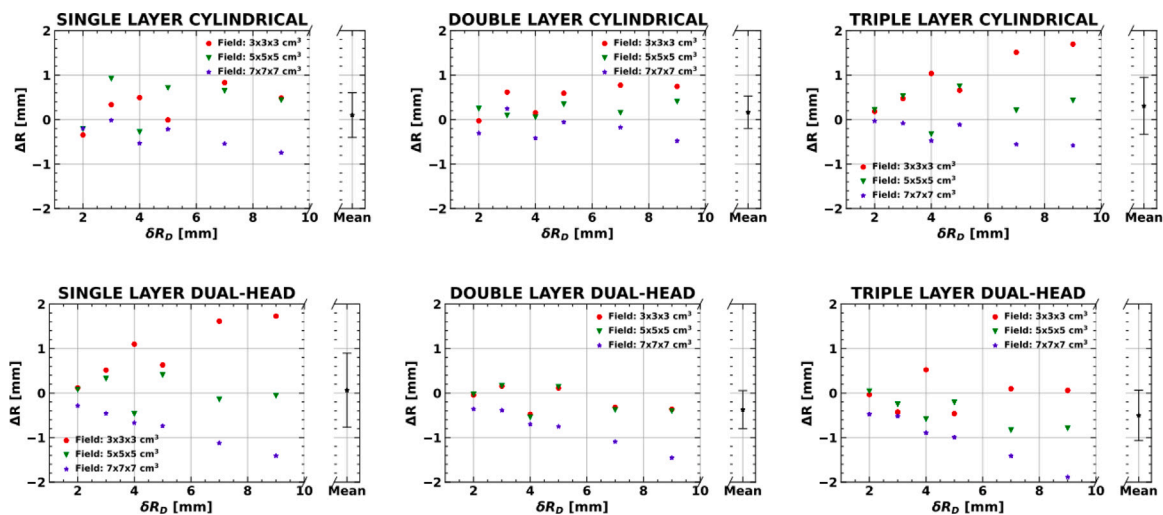


Fig. 7. ΔR for all six geometries of the J-PET scanner investigated for SOBP irradiations with different fields size. Top row shows the results for cylindrical geometries and the bottom for the dual-head setups. The columns from left to right present the results for the single, double and triple layer scanner geometries.

4. Discussion

The ΔR values, the difference between the range shift in the dose and the range shift as estimated from the reconstructed activity distributions, are mostly smaller than the expected J-PET resolution, which is at the level of a few millimeter [25]. It is expected that the spatial resolution on range monitoring will be the same. Therefore, it can be concluded that following experimental verification, in principle, all investigated configurations could be considered for practical application in proton range monitoring. However, it should be stressed, that the investigations presented here were performed in a uniform phantom. Further studies to assess the feasibility of range detection for heterogeneous Intensity-Modulated Proton Therapy treatment plans in non-uniform patient tissue are required [42]. Potentially small differences between the investigated geometries observed here for simplified quality assurance settings may result in much more significant differences in a clinical setting. In this context, both precision and sensitivity should be considered essential factors for geometry optimization, taking into account that the general rule for PET imaging is that greater statistics will improve the reconstructed image quality.

The presented results, considering both sensitivity and precision, as well as the cost-effectiveness of J-PET based configurations, indicate

that the double-layer cylindrical and triple-layer dual-head configurations are the most promising for range monitoring in the treatment room. The triple layer dual-head geometry has the greatest efficiency factor \bar{H} (as it is shown in Table 1) among the scanners with 24 modules. This is the number of modules currently available and undergoing commissioning with the modular prototype of the system. The double-layer cylindrical geometry is the envisioned final Total-Body J-PET geometry [25] and would potentially benefit from the experience of the J-PET group in scanner construction and future operation. Note that the double-layer setup has a sensitivity increase of 300% with respect to the single-layer setup, while the triple-layer setup has a sensitivity increase of about 70% with respect to the double-layer configuration, pointing to the double-layer scanner as the most cost-effective configuration.

Direct comparison with other PET range monitoring systems is not straightforward due to the differences in the experimental setup, e.g. phantom size or irradiation plans. Recently, the mobile PET system DoPET, developed at the University of Pisa, Italy [52,53], has been investigated for the application of range monitoring in proton therapy. Various phantoms were irradiated and PET signal was acquired immediately after the irradiation for five minutes, mimicking the in-room range monitoring approach. Their experiments and Monte Carlo simulations with FLUKA [54,55] revealed that the efficiency factor

(number of coincidences per primary protons) is at the level of $\eta = 2.85 \cdot 10^{-5}$. The double- and triple-layer J-PET scanners investigated in this study have the sensitivity of the same order of magnitude as the DoPET system. However, a comparison of the precision in range measurement is challenging, considering the different irradiation and PET acquisition scenarios (phantoms, treatment plan, acquisition protocol), and is beyond the scope of this manuscript. In comparison to DoPET, the J-PET systems show similar sensitivity, while its advantages are the cost-effectiveness and modular design, which enable construction systems capable of various PET acquisition scenarios and facilitate installation in treatment rooms of different designs.

The uncertainties of the presented simulations study are related to the assumptions made regarding irradiation and scanner. We applied an artificial discretization of the plastic strip into a hundred 5-mm long pseudo-crystals, which in the first approximation is in agreement with the expected resolution of the currently produced 3rd generation J-PET scanner that uses wave length shifters (WLS) that offer improved time resolution [25,47]. Minor uncertainties may relate to the physics modelling used for the simulation of the activity production and propagation of the 511 keV annihilation photons [43]. Based on the clinical protocols used in CCB Krakow proton therapy centre, we have also assumed 2 min PET acquisition time [42], while the detected PET signal may substantially vary when modifying acquisition time. The uncertainties related to the PET image reconstruction are related to, e.g., sensitivity correction, normalization, attenuation correction, number of iterations used in the reconstruction, post-reconstruction image filtering. To simplify the presented preliminary analysis, we have omitted the propagation of the uncertainty related to the fitting of the activity profile fall-off to the δR and σR_D values. The simulated phantom irradiations were performed with relatively high doses of 4 Gy (SBP) and 8 Gy (SOBP), characteristic of the hypofractionated treatments, where range monitoring is of particular importance. Range monitoring of patients with 2 Gy fraction doses will result in lower coincidence statistics and is being further investigated in [42].

For the assessment and characterization of diagnostic PET scanners, NEMA norms [56] are used. We propose that the sensitivity and precision analysis presented here be the first step towards introducing similar norms for the evaluation of PET scanners for proton beam range monitoring. This evaluation should, furthermore, consider such aspects as cost-effectiveness and the suitability of the technology for intra-treatment PET imaging. We believe that the ProTheRaMon framework, offering a standardized simulation and image reconstruction environment, may be helpful for reliable comparison of different setups. A consensus and guidelines for the evaluation of PET-based range monitoring techniques would be of great benefit in fostering future developments in proton beam range monitoring and in its translation into the clinic.

5. Conclusions

In this paper, the feasibility of the J-PET detector for PET-based proton beam therapy range monitoring was investigated. Six different scanner geometries were tested by means of simulations. Relative efficiency and range assessment precision were computed in order to find the optimal geometrical configuration.

The study reveals that considering the sensitivity, precision and cost-effectiveness of different approaches, the most promising for the intra-treatment clinical application are the double-layer cylindrical and triple-layer dual-head configurations. Among the scanners with 24 modules of the J-PET detector, the best results were obtained with the triple-layer dual-head system. All the systems show the feasibility of range assessment with precision at the level of 1 mm for both SPB and SOBP irradiations. Experimental validation of the presented results is needed and ongoing.

Acknowledgements

This work was supported by the National Centre for Research and Development (NCBiR), Poland, grant no. LIDER/26/0157/L-8/16/NCBR/2017. Calculations were performed on the Ziemowit computer cluster in the Laboratory of Bioinformatics and Computational Biology at the Biotechnology Centre, the Silesian University of Technology, created in the EU Innovative Economy Programme POIG.02.01.00-00-166/08 and expanded in the POIG.02.03.01-00-040/13 project. Development of ProTheRaMon was supported by the National Centre for Research and Development (NCBiR), Poland, grant no. LIDER/43/0222/L-12/20/NCBR/2021. We acknowledge also support by the Foundation for Polish Science, Poland through the TEAM POIR.04.04.00-00-4204/17 program, the National Science Centre of Poland through grant 2021/42/A/ST2/00423, and the SciMat and qLife Priority Research Areas budget under the program *Excellence Initiative - Research University* at the Jagiellonian University, Poland, and Jagiellonian University project no. CRP/0641.221.2020.

Declaration of competing interest

The Authors declare no conflict of interest.

References

- [1] Paganetti H. *Proton therapy physics*, vol. 103, Boston, USA: CRC Press Taylor & Francis Group; 2012.
- [2] Durante M, Orecchia R, Loeffler J. Charged-particle therapy in cancer: clinical uses and future perspectives. *Nat Rev Clin Oncol* 2017;14:483.
- [3] Nystrom H, Jensen M, Nystrom P. Treatment planning for proton therapy: what is needed in the next 10 years? *Br J Radiol* 2020;93:20190304.
- [4] Krimmer J, Dauvergne D, Létang J, Testa É. Prompt-gamma monitoring in hadrontherapy: A review. *Nucl Instrum Methods Phys Res A* 2018;878:58–73.
- [5] Pennazio F, et al. Proton therapy monitoring: spatiotemporal emission reconstruction with prompt gamma timing and implementation with PET detectors. *Phys Med Biol* 2022;67:065005.
- [6] Missaglia A, Bourkadi-Idrissi A, Casamichiela F, Mazzucconi D, Carminati M, Agosteo S, et al. Prompt-gamma fall-off estimation with C-ion irradiation at clinical energies, using a knife-edge slit camera: A Monte Carlo study. *Phys Med* 2023;107:102554.
- [7] Yamamoto S, Yabe T, Akagi T, Yamaguchi M, Kawachi N, Kamada K, et al. Prompt X-ray imaging during irradiation with spread-out bragg peak (SOBP) beams of carbon ions. *Phys Med* 2023;109:102592.
- [8] Traini G, et al. Review and performance of the Dose Profiler, a particle therapy treatments online monitor. *Phys Med* 2019;65:84–93.
- [9] Battistoni G, et al. Measurement of charged particle yields from therapeutic beams in view of the design of an innovative hadrontherapy dose monitor. *J Instrum* 2015;10:C02032.
- [10] Marafini M, et al. MONDO: a neutron tracker for particle therapy secondary emission characterisation. *Phys Med Biol* 2017;62:3299.
- [11] Bashkirev V, Schulte R, Johnson R, PM. In-beam range verification with scattered particles registered with a particle CT scanner. In: 59th AAPM meeting. 2017.
- [12] Bauer J, et al. Implementation and initial clinical experience of offline PET/CT-based verification of scanned carbon ion treatment. *Radiother Oncol* 2013;107:218–26.
- [13] Bisogni M, et al. INSIDE in-beam positron emission tomography system for particle range monitoring in hadrontherapy. *J Med Imaging* 2016;4:011005.
- [14] Ferrero V, et al. Online proton therapy monitoring: clinical test of a Silicon-photodetector-based in-beam PET. *Sci Rep* 2018;8:4100.
- [15] Lang K. Towards high sensitivity and high-resolution PET scanners: imaging-guided proton therapy and total body imaging. *Bio-Algorithms Med-Syst* 2022;18:96–106.
- [16] Handrack J, et al. Sensitivity of post treatment positron emission tomography/computed tomography to detect inter-fractional range variations in scanned ion beam therapy. *Acta Oncol* 2017;56:1451–8.
- [17] Fiorina E, et al. Detection of inter-fractional morphological changes in proton therapy: a simulation and in-vivo study with the INSIDE in-beam PET. *Front Phys* 2020;8:660.
- [18] Baran J, Gajewski J, Pawlik-Niedźwiecka M, Moskal P, Ruciński A. Studies of J-PET detector to monitor range uncertainty in proton therapy. In: 2019 IEEE nuclear science symposium and medical imaging conference. IEEE; 2019, p. 1–4.
- [19] Ruciński A, et al. Investigations on physical and biological range uncertainties in Krakow proton beam therapy centre. *Acta Phys Polon B* 2020;51:9–16.
- [20] Tashima H, et al. Development of a small single-ring OpenPET prototype with a novel transformable architecture. *Phys Med Biol* 2016;61:1795.

- [21] Yamaya T, Tashima H. Openpet enabling PET imaging during radiotherapy. In: Personalized pathway-activated systems imaging in oncology. Springer; 2017, p. 55–84.
- [22] Yoshida E, et al. Development of a whole-body dual ring OpenPET for in-beam PET. *IEEE Trans Radiat Plasma Med Sci* 2017;1:293–300.
- [23] Crespo P, Shakinir G, Enghardt W. On the detector arrangement for in-beam PET for hadron therapy monitoring. *Phys Med Biol* 2006;51:2143.
- [24] Moskal P, et al. Testing CPT symmetry in ortho-positronium decays with positronium annihilation tomography. *Nature Commun* 2021;12:5658.
- [25] Moskal P, et al. Simulating NEMA characteristics of the modular total-body J-PET scanner—an economic total-body PET from plastic scintillators. *Phys Med Biol* 2021;66:175015.
- [26] Vandenberghe S, Moskal P, Karp J. State of the art in total body PET. *EJNMMI* 2020;7.
- [27] Moskal P, et al. Time resolution of the plastic scintillator strips with matrix photomultiplier readout for J-PET tomograph. *Phys Med Biol* 2016;61:2025.
- [28] Moskal P, Stepień E. Prospects and clinical perspectives of total-body PET imaging using plastic scintillators. *PET Clin* 2020;15:439–52.
- [29] Kowalski P, et al. Estimating the NEMA characteristics of the J-PET tomograph using the GATE package. *Phys Med Biol* 2018;63:165008.
- [30] Moskal P, et al. Feasibility study of the positronium imaging with the J-PET tomograph. *Phys Med Biol* 2019;64:055017.
- [31] Moskal P, et al. Positronium imaging with the novel multiphoton PET scanner. *Sci Adv* 2021;7:eabh4394.
- [32] Hiesmayr B, Moskal P. Witnessing entanglement in compton scattering processes via mutually unbiased bases. *Sci Rep* 2019;9:1–14.
- [33] Sharma S, Kumar D, Moskal P. Decoherence puzzle in measurements of photons originating from electron-positron annihilation. 2022, arXiv preprint arXiv:2210.08541.
- [34] Shopa RY, et al. Optimisation of the event-based TOF filtered back-projection for online imaging in total-body J-PET. *Med Image Anal* 2021;73:102199.
- [35] Raczyński L, et al. 3D TOF-PET image reconstruction using total variation regularization. *Phys Med* 2020;80:230–42.
- [36] Vozenin M-C, Bourhis J, Durante M. Towards clinical translation of FLASH radiotherapy. *Nat Rev Clin Oncol* 2022;19:791–803.
- [37] Niedźwiecki S, et al. J-PET: a new technology for the whole-body PET imaging. *Acta Phys Polon B* 2017;48:1567.
- [38] Kapłon Ł. Technical attenuation length measurement of plastic scintillator strips for the total-body J-PET scanner. *IEEE Trans Nucl Sci* 2020;67:2286–9.
- [39] Korcyl G, et al. Evaluation of single-chip, real-time tomographic data processing on FPGA SoC devices. *IEEE Trans Med Imaging* 2018;37:2526–35.
- [40] Shakinir G, et al. Implementation and workflow for PET monitoring of therapeutic ion irradiation: a comparison of in-beam, in-room, and off-line techniques. *Phys Med Biol* 2011;56:1281.
- [41] Parodi K. Latest developments in in-vivo imaging for proton therapy. *Br J Radiol* 2020;93:20190787.
- [42] Brzeziński K, et al. Detection of range shifts in proton beam therapy using the J-PET scanner: a patient simulation study. *Phys Med Biol* 2023;68:145016.
- [43] Borys D, et al. ProTheRaMon—a GATE simulation framework for proton therapy range monitoring using PET imaging. *Phys Med Biol* 2022;67:224002.
- [44] Gajewski J, Garbacz M, Chang C-W, Czerska K, Durante M, Krahn N, et al. Commissioning of GPU-accelerated Monte Carlo code FRED for clinical applications in proton therapy. *Front Phys* 2021;8:403.
- [45] Moskal P, et al. Test of a single module of the J-PET scanner based on plastic scintillators. *Nucl Instrum Methods Phys Res A* 2014;764:317–21.
- [46] Merlin T, et al. CASToR: a generic data organization and processing code framework for multi-modal and multi-dimensional tomographic reconstruction. *Phys Med Biol* 2018;63:185005.
- [47] Smyrski J, et al. Measurement of gamma quantum interaction point in plastic scintillator with WLS strips. *Nucl Instrum Methods Phys Res A* 2017;851:39–42.
- [48] Camarlinghi N, et al. An in-beam PET system for monitoring ion-beam therapy: test on phantoms using clinical 62 MeV protons. *J Instrum* 2014;9:C04005.
- [49] Kraan AC, et al. First tests for an online treatment monitoring system with in-beam PET for proton therapy. *J Instrum* 2015;10:C01010.
- [50] Kraan A. Range verification methods in particle therapy: underlying physics and Monte Carlo modeling. *Front Oncol* 2015;5:150.
- [51] Min CH, Zhu X, Winey BA, Grogg K, Testa M, El Fakhri G, et al. Clinical application of in-room positron emission tomography for in vivo treatment monitoring in proton radiation therapy. *Int J Rad Oncol Biol Phys* 2013;86:183–9.
- [52] Kraan A, et al. Analysis of in-beam PET time-profiles in proton therapy. *J Instrum* 2019;14:C02001.
- [53] Topi A, et al. Monitoring proton therapy through in-beam PET: An experimental phantom study. *IEEE Trans Radiat Plasma Med Sci* 2019;4:194–201.
- [54] Battistoni G, et al. Overview of the FLUKA code. *Ann Nucl Energy* 2015;82:10–8.
- [55] Augusto R, et al. An overview of recent developments in FLUKA PET tools. *Phys Med* 2018;54:189–99.
- [56] NEMA. NEMA Standards publication NU 2-2018: Performance measurements of positron emission tomographs (PET). National Electrical Manufacturers Association (NEMA NU 2-2018; 2018).